

Magnetic-domain-dependent pseudogap induced by Fermi surface nesting in a centrosymmetric skyrmion magnet

Yuyang Dong,¹ Yuto Kinoshita,¹ Masayuki Ochi,^{2,3} Ryu Nakachi,⁴
Ryuji Higashinaka,⁴ Satoru Hayami,⁵ Yuxuan Wan,¹ Yosuke Arai,¹
Soonsang Huh,¹ Makoto Hashimoto,⁶ Donghui Lu,⁶ Masashi Tokunaga,^{1,7}
Yuji Aoki,⁴ Tatsuma D. Matsuda,⁴ and Takeshi Kondo^{1,7,*}

¹*Institute for Solid State Physics, The University of Tokyo, Kashiwa, Chiba 277-8581, Japan*

²*Department of Physics, Osaka University, Toyonaka, Osaka 560-0043, Japan*

³*Forefront Research Center, Osaka University, Toyonaka, Osaka 560-0043, Japan*

⁴*Department of Physics, Tokyo Metropolitan University, Tokyo 192-0397, Japan*

⁵*Department of Physics, Hokkaido University, Sapporo 060-0810, Japan*

⁶*Stanford Synchrotron Radiation Lightsource,
SLAC National Accelerator Laboratory, Menlo Park, CA 94025, USA*

⁷*Trans-scale Quantum Science Institute,
The University of Tokyo, Tokyo 113-0033, Japan*

arXiv:2307.08000v1 [cond-mat.mtrl-sci] 16 Jul 2023

* kondo1215@issp.u-tokyo.ac.jp

Skymions in non-centrosymmetric materials are believed to occur due to the Dzyaloshinskii-Moriya interaction. In contrast, the skymion formation mechanism in centrosymmetric materials remains elusive. Among those, Gd-based compounds are the prototype compounds; however, their electronic structure is not uncovered, even though it should be the foundation for elucidating the skymion mechanism. Here, we reveal the intrinsic electronic structure of GdRu_2Si_2 for the first time by magnetic domain selective measurements of angle-resolved photoemission spectroscopy (ARPES). In particular, we find the robust Fermi surface (FS) nesting, consistent with the q -vector detected by the previous resonant X-ray scattering (RXS) measurements. Most importantly, we find that the pseudogap is opened at the nested portions of FS at low temperatures. The momentum locations of the pseudogap vary for different magnetic domains, most likely having a direct relationship with the screw-type spin modulation that changes direction for each domain. Intriguingly, the anomalous pseudogap disconnects the FS to generate Fermi arcs with 2-fold symmetry. These results indicate the significance of Ruderman-Kittel-Kasuya-Yosida (RKKY) interaction, in which itinerant electrons mediate to stabilize the local magnetic moment, as the mechanism for the magnetism in the Gd-based skymion magnets. Our data also predict that the momentum space where the pseudogap opens is doubled (or Fermi arcs shrink) and thereby stabilizes the skymion phase under a magnetic field. Furthermore, we demonstrate the flexible nature of magnetism in GdRu_2Si_2 by manipulating magnetic domains with a magnetic field and temperature cyclings, providing a possibility of future application for data storage and processing device with centrosymmetric skymion magnets.

Magnetic skymions are generated as particles with spiral spin textures due to the non-trivial topology in real space. Since their discovery about a decade ago, magnetic skymions have attracted enormous research interest because they exhibit various exotic phenomena and a high potential for the spintronic device application [1–5]. While most magnetic skymion materials are non-centrosymmetric [6–9], several centrosymmetric systems yielding skymion lattice have been discovered in the past few years [10–15]. One significant feature of skymions in centrosymmetric systems is their tiny size (<4 nm), much smaller than that in non-centrosymmetric systems (generally around several tens of nanometers) [16]. Such a smaller size of skymion can generate more robust electrodynamic responses originating from the quantum mechanical Berry phase, being desirable for future high-density data storage and processing devices [17–21].

The most well-acknowledged family of centrosymmetric skymion magnets are Gd-based skymion materials: Gd_2PdSi_3 [10], $\text{Gd}_3\text{Ru}_4\text{Al}_{12}$ [11], and GdRu_2Si_2 [12]. In particular,

GdRu₂Si₂ is known as the material forming the smallest size (~ 1.9 nm) of skyrmions among all materials hosting skyrmions. While the formation mechanism of skyrmions in non-centrosymmetric materials is widely agreed to be the Dzyaloshinski-Moriya interaction, it remains a challenge to clarify the corresponding mechanism in the centrosymmetric Gd-based materials.

Several theoretical works have proposed geometrical frustration [22, 23] or orbital frustration [24] as key for the skyrmion lattice state in Gd-based skyrmion materials; some others believe the requirement of RKKY interaction [25–28] or higher-order spin interactions [29–31]. Either of these mechanisms would significantly modify the electronic structure, thus its detailed observation could bring the breakthrough to the argument of the skyrmion formation mechanism in centrosymmetric materials. Such a study, however, has not been done to date while strongly desired. ARPES measurements are the most direct way of determining the electronic structure of matter, which, however, is not straightforward in the investigation of the Gd-based skyrmion materials. The difficulty is that structural terminations on the sample surface and magnetic domains can greatly complicate the ARPES signals. Extremely careful measurements solving these complications are required to unveil the intrinsic electronic structure associated with the fascinating magnetic order in those compounds.

In this study, we reveal the electronic structure in the Gd-based centrosymmetric skyrmion magnets for the first time by using the ARPES technique which solves the difficulties due to both surface terminations and magnetic domains. Among the three Gd-based skyrmion materials, in particular, we selected GdRu₂Si₂ as a research target because not only of its simplest crystal structure [32–34] but also of a fascinating property that can form the smallest skyrmion ever [12]. Magnetic phases of GdRu₂Si₂ have previously been studied by RXS and scanning tunneling microscope (STM) experiments [12, 35, 36]. The emergence of a topologically non-trivial skyrmion lattice state (Phase II) requires both low temperatures (below 20 K) and a magnetic field (within a narrow range above 2 T). The magnetic field is not allowed in ARPES measurements, so we investigate the electronic structure only of the ground state at a zero magnetic field (Phase I). Nevertheless, it is crucial to investigate the ground state for elucidating the skyrmion mechanism because the ground and skyrmion phases (Phase I and Phase II, respectively) share similar magnetic modulation \mathbf{q} -vectors: $\mathbf{q}_1 \sim (0.22, 0, 0)$ and $\mathbf{q}_2 \sim (0, 0.22, 0)$. Here, 0.22 r.l.u. corresponds to about 0.33 \AA^{-1} . Note that the skyrmion is thought to be formed by the superposition of multiple \mathbf{q} -vectors. The formation mechanism of these \mathbf{q} -vectors should be reflected in the electronic structure at the ground state, and thus its direct observation by ARPES is critical to understanding the skyrmion mechanism in centrosymmetric materials.

We selectively observe Si-termination and Gd-termination on the crystal surface of GdRu₂Si₂ cleaved along the (001) plane by ARPES using synchrotron light of a small beam

spot ($\sim 40 \times 10 \mu\text{m}^2$). Figure 1A maps the photoemission intensity near E_F obtained by scanning the beam spot every $20 \mu\text{m}$ over the cleavage surface. Here, we use the photon energy of 148 eV allowing the resonant photoemission [37] to obtain a better contrast in the intensity map. This photon energy also corresponds to the k_z value at the Γ point. A clear contrast of bright or dark indicates different local densities of states (LDOS) near E_F , distinguishing two kinds of areas either for Gd-termination or Si-termination. To identify the correspondence between each area and termination, core-level photoemission is performed (Fig. 1B) for these two areas: the green spot (bright area) and the purple spot (dark area) marked in Fig. 1A. The intensity of the Si $2p$ peak is lower than that of the Gd $4f$ peak at the green spot. Inversely, the former is higher than the latter at the purple spot. This result identifies the green and purple spots as Gd-termination and Si-termination, respectively.

Next, we conduct ARPES measurements for these two terminations separately. The Si-termination (Fig. 1D) exhibits two circle-shaped FS sheets within a large windmill-shaped FS sheet centered at Γ point. In contrast, these characteristic features are not observed for the Gd-termination (Fig. 1C). Instead, much higher intensities are detected at the center Γ point. Apparent discrepancies between the two domains are also found in the band dispersion. Figure 1E,F is the band dispersions of Gd-termination and Si-termination, respectively, passing through the Γ point. The overall difference between the two is apparent; for instance, there are some sharp bands near E_F in Si-termination (Fig. 1F) while these bands are missing in Gd-termination (Fig. 1E). These discrepancies allow us to easily distinguish the two domains during ARPES measurements.

For a study of the skyrmion mechanism in GdRu_2Si_2 , it is crucial to extract the intrinsic bulk information from these data. As a reference, the bulk-state FS calculated with density functional theory (DFT) is displayed in Fig. 1G. The FS of terminations is composed of surface and bulk signals. Therefore, the common part of FS observed from Gd-termination and Si-termination should be for the intrinsic bulk state. Such features are indeed found in the data. The ones particularly remarkable are the parallel FS observed at the corner of the Brillouin zone (BZ) in both terminations. Figure 1H overlays the momentum distribution curves (MDCs) at E_F along k_x crossing the BZ corner (dotted lines in Fig. 1C and Fig. 1D) for Gd-termination and Si-termination. A good agreement is obtained in the peak positions between the two curves, validating that the parallel FS is for the bulk state. We focus our study on this part of FS.

We compare side by side the in-plane FS map at $k_z = 0$ by the ARPES measurements with 94 eV photons (Fig. 2A) and the DFT calculations (Fig. 2B). The agreement between the two is excellent, particularly in the parallel segments around the BZ corner. Most importantly, we find robust FS nesting which almost perfectly matches the \mathbf{q} -vectors of magnetic modulation reported (green and blue arrows in Fig. 2B). In Fig. 2C, we plot

an ARPES dispersion measured along a momentum cut connecting two BZ corners (black arrow in Fig. 2A). On the top panel, the MDC at E_F is extracted. Sharp spectral peaks pointing to the k_F locations allow us to precisely determine the nesting vector (green arrows in Fig. 2C). Similarly, we observe band dispersions along k_x at different k_y positions marked by green circles in the zoomed FS map (Fig. 2D) of the red rectangular region in Fig. 2A. In Fig. 2E, the nesting wave vectors determined by ARPES (green circles) are compared with those of our DFT calculations (red line), and the lengths of \mathbf{q} -vectors reported by RXS measurements [12]. These three are found to almost perfectly match each other at \mathbf{q} -vector of $\sim 0.33 \text{ \AA}^{-1}$ along k_x .

Next, we examine the FS nesting along the k_z direction. The k_z value of the in-plane FS observed can be controlled by changing photon energies. In Fig. 2F,G, we plot in-plane FS maps around the zone corner measured at photon energies over a wide range from 94 eV to 67 eV covering the entire BZ along k_z . The direction of the parallel FS is rotated by 90° when the observed k_z is shifted by half the BZ distance (Fig. 2F). This k_z variation justifies that the ARPES signals are indeed for the bulk state. At the same time, it may worsen the nesting condition along the k_z direction. Importantly, however, the FS nesting of the same \mathbf{q} -vector is valid in the entire BZ along k_z , as long as focusing on the center cut of the nested segments (dashed white lines in Fig. 2G). This is more clearly demonstrated in Fig. 2H by plotting the corresponding MDCs at different photon energies covering the entire BZ along k_z . The nesting wave vector marked by the green arrow is almost constant in length at different k_z positions. Our DFT calculations reproduce the FS which is almost perfectly nested along the entire k_z (Fig. 2I). These results along k_z are summarized in Fig. 2J; all three of the nesting wave vectors determined by ARPES and DFT calculations, and \mathbf{q} -vector observed by RXS show almost perfect agreement with each other. Our results, therefore, evidence the robust FS nesting in both the in-plane and out-of-plane directions, indicating that itinerant electrons near E_F play an important role; more specifically, the interaction between the magnetic moments would be mediated by the RKKY interaction in which the FS nesting essentially involves. This notion will be further solidified in the experimental investigations presented below.

Temperature-dependent behavior of the electronic structure is investigated to understand the phase transition in GdRu_2Si_2 across the Néel temperature (T_N) of 46 K. Figure 3A shows a band dispersion across the nested FS at a low temperature (10 K) deep below T_N . Here, we use 148 eV photons, which correspond to $k_z = 0$. The magnified band map in Fig. 3B (a green-dotted rectangular region in Fig. 3A) exhibits two band dispersions. The band on the left (red arrow) participates in the FS nesting, while the other on the right (blue arrow) does not. Interestingly, we find a weight loss of spectra near E_F in the nesting band due to the opening of the pseudogap, as schematically illustrated in Fig. 3D. The intensity loss toward

E_F results in a penpoint-like shape in the color map. The pseudogap is, in contrast, absent in the non-nesting band. We also confirm in Fig. 3B that the pseudogap is closed at a high temperature ($T = 50$ K) above T_N . Note here that the data do not exhibit band splitting at low temperatures below T_N as proposed by orbital frustration theory [24]. If there were band splitting, the nesting wave vector should change between low and high temperatures; it, however, does not occur. This result is extremely important in identifying the appropriate one from several proposed theories of the skyrmion mechanism in this compound.

To better understand the relationship between the pseudogap and the phase transition, we examine in Fig. 3F the detailed temperature dependence of energy distribution curves (EDCs) at k_F for the nesting band (red arrow in Fig. 3B,C). The pseudogap magnitude is estimated to be about 100 meV at 10 K. With increasing temperature, the pseudogap decreases and eventually closes at high temperatures (Fig. 3F). This gets clearer by symmetrizing EDCs about E_F (Fig. 3G). Two peaks merge into one peak at elevated temperatures, indicating that the gap closes. In contrast, the spectra at k_F for the non-nesting band (blue arrow in Fig. 3B,C) do not open a gap and they only get broadened at elevated temperatures due to the thermal broadening (Fig. 3H,I). These results are further examined in Fig. 3E by extracting the spectral weight near E_F (color-hatched area in Fig. 3G,I), which is most sensitive to the gap filling and the thermal broadening. The spectral weight of the nesting band (red) remarkably increases up to T_N , saturating in the paramagnetic (PM) phase. In contrast, the spectral weight for the non-nesting band (blue) decreases in a rather monotonic fashion as temperature increases due to the thermal broadening. The pseudogap is, therefore, closely related to the magnetic order in GdRu_2Si_2 . It also explains the upturn in the resistivity behavior previously reported [34] and for our samples (Supplementary Fig. S4).

We perform the magnetic domain-selective measurements to fully understand the magnetic band structure of GdRu_2Si_2 . Such measurements require instrumental technology that combines a focused beam and a sophisticated sample manipulator enabling stable scan over the sample surface, and those became available only recently in the ARPES research. Very intriguingly, we find that the pseudogap has a domain dependence: only one of two \mathbf{q} -vectors (either k_x or k_y) involve the pseudogap opening.

Figure 4A shows the spatial mapping of photoemission intensity near E_F on the sample surface of GdRu_2Si_2 . One can distinguish Si-termination and Gd-termination from high and low intensities, respectively. We select 20 spots that are evenly spaced and cover both terminations for the ARPES measurements. In Fig. 4D-K, we display the nesting bands measured at 10 K along the BZ corners for 4 spots (Position I, II, III, IV, marked in Fig. 4A) as examples. Here, the left two rows are for Gd-termination and the right two rows are for Si-termination. For each spot, we measured two different momentum cuts: the horizontal

cut along k_x (cut H) and the vertical cut along k_y (cut V), which are separately displayed on the top and low panels. We note here that these two cuts were measured at the same experimental geometry for a fair comparison (Supplementary Section V and Fig. S5). The pseudogap is observed for all the spots. Interestingly, however, we find that only one of the paired two cuts (cut H or cut V) shows the opening of the pseudogap; that is, some spots (Position I, III) open the pseudogap only on cut H, but the others (Position II, IV) only on cut V, as illustrated in Fig. 4B,C with schematic FSs, respectively.

These data provide two implications. One is that the abnormal Fermi arc emerges due to the pseudogap that opens only in partial momentum space. Second is that the electronic structure breaks the 4-fold symmetry of the crystal structure, becoming the 2-fold symmetry in the ground state (Phase I). This causes two kinds of magnetic domains with the pseudogap opened in different directions. Importantly, both the red situation of Fig. 4B (Position I, III) and the blue situation of Fig. 4C (Position II, IV) can be observed in the same termination either of Gd-termination (Position I, II) or Si-termination (Position III, IV). Therefore, the two kinds of magnetic domains are independent of terminations and they should originate from the intrinsic bulk property. This is more clearly demonstrated in Fig. 4A by distinguishing all the measured 20 spots with red and blue. It is revealed that magnetic domains are quite large and their shapes and locations are independent of the terminations.

The two-fold electronic structure revealed by ARPES is compatible with the anisotropic magnetic double- \mathbf{q} state observed by RXS. The previous RXS measurements uncovered that the magnetic structure of Phase I at a zero magnetic field is formed by the superposition of the screw spin modulation $\mathbf{q}_1 = (0.219, 0, 0)$ [or equivalent $\mathbf{q}_1 = (0, 0.219, 0)$] and the sinusoidal spin modulation $\mathbf{q}_2 = (0, 0.224, 0)$ [or equivalent $\mathbf{q}_2 = (0.224, 0, 0)$] [36]. The difference in the length of these two perpendicular \mathbf{q} -vectors is so tiny that it is within the measurement error of the nesting wave vector by ARPES. Each parallel part of FS can, therefore, be connected by both \mathbf{q}_1 and \mathbf{q}_2 . Our ARPES results that the pseudogap opens along only one of k_x or k_y direction (green arrows in Fig. 4B,C) means that only one of the magnetic modulations (either screw-type \mathbf{q}_1 or sinusoidal-type \mathbf{q}_2) generates the pseudogap.

We conjecture that the pseudogap is generated by the screw spin modulation, not the sinusoidal spin modulation. The spin moments of the screw-type modulation have equal lengths and they oscillate not only in the (001) plane but also along the [001] direction (Fig. 5H). On the other hand, the spin moments of sinusoidal-type modulation have a shorter length on average than the screw-type and they oscillate only in the (001) plane but not along the [001] direction (Fig. 5H). Therefore, the screw spin modulation should be more strongly coupled with the electronic structure than the sinusoidal spin modulation [38]. The skyrmion lattice is formed as the superposition of two perpendicular screw spin modulations. Hence,

our results suggest that the pseudogap opens at a large portion of the nested FS simultaneously connected by two screw-type \mathbf{q} -vectors of each vertical and horizontal direction, energetically stabilizing the skyrmion state under a magnetic field.

To investigate the properties of the magnetic domains further, we perform polarizing microscopy measurements. We use the same sample pieces measured by ARPES for the measurements to clarify the correspondence between the results of these two different experimental techniques. Figure 5A,C show the spatial mapping of photoemission intensity obtained from two sample pieces (sample #1 and sample #2). The red and blue spots mark different magnetic domains distinguished by ARPES via observing the pseudogap which opens at different momenta. For the same sample pieces, we also took the polarizing microscopy images (Fig. 5B,D for sample #1 and sample #2, respectively). Each image plots the intensity difference between 10 K (Phase I) and 50 K (PM) to extract only the signals due to the magnetic order. The magnetic domains determined by ARPES match perfectly well those by the polarizing microscopy image.

Finally, we demonstrate unique manipulations of the magnetic domains in GdRu_2Si_2 by a magnetic field and temperature cyclings in Phase I. Figure 5E shows a schematic phase diagram with Fig. 5F-I representing magnetic ordering in each phase, adopted from previous RXS research [36]. Both of the magnetic field and temperature cyclings excite the system to the one with a 4-fold symmetry and then take back it to the one with a 2-fold symmetry. For the magnetic field cycling, we used a pulsed field with a width of 4.6 ms. The polarizing microscopy images obtained by a series of experiments are shown in Fig. 5J-5M. All the images are subtracted by the image at 50 K (PM) as background. As the first procedure, the temperature was decreased from 50 K (PM) to 10 K (Phase I) without a magnetic field (Fig. 5J: ④→①). Two domains (blue and white areas) clearly appear at 10 K in Phase I. Secondly, the magnetic state was excited from Phase I to Phase II (skyrmion state) by a pulsed magnetic field, which comes back to Phase I in a short time (Fig. 5K: ①→②→①). We find a large number of domain bubbles to appear near the original domain boundary, although the main parts of the domains remain almost unchanged. This indicates a competition between the flexibility of the skyrmion state and the stiffness of the memorized magnetic order during the magnetic field cycling. Thirdly, the magnetic state was excited from Phase I to Phase III and then taken back to Phase I again by a pulsed magnetic field (Fig. 5L: ①→③→①). Much smaller bubble-like domains appear and their distribution is completely random, indicating that the memory of the original domains is erased. Lastly, the temperature is increased from 10 K (Phase I) to 50 K (PM) and then decreased to 10 K (Phase I) again without an external magnetic field (Fig. 5M: ①→④→①). Intriguingly, the profile and distribution of magnetic domains are perfectly restored to the original ones (Fig. 5J).

Notably, the bubbles of magnetic domains are found to appear not only by using a pulsed field but also by using a static field as the magnetic field cycling (supplementary Fig. S8). Our results, therefore, demonstrate that the magnetic domain patterns in Phase I can be easily manipulated by applying magnetic fields (regardless of static and pulsed magnetic fields), while they are robust against temperature cycling and can be perfectly restored. The dual character of magnetism which can erase and restore the memorized domain patterns by magnetic field and temperature cyclings is unknown in other magnetic materials. Hence, this should be a unique feature of GdRu_2Si_2 and should be tightly related to the skyrmion formation mechanism, perhaps due to the higher-order spin interactions between different magnetic modulations. Our findings about the magnetic domain manipulation with field and temperature would be insightful for future engineering applications for data storage and processing with centrosymmetric skyrmion magnets.

Acknowledgements

We thank K. Kuroda and T. Taniuchi for fruitful discussion on the results, and also thank T. Yajima for XRD measurements. Use of the Synchrotron Radiation Lightsource, SLAC National Accelerator Laboratory, is supported by the U.S. Department of Energy, Office of Science, Office of Basic Energy Sciences under Contract No. DE-AC02-76SF00515. This work was supported by the JSPS KAKENHI (Grants Numbers. JP21H04439, JP19H00651, JP22K03517, JP21H01037, and JP23H04869), by the Asahi Glass Foundation, by MEXT Q-LEAP (Grant No. JPMXS0118068681), by JST PRESTO (Grant No. JPMJPR20L8), by The Murata Science Foundation, and by Tokyo Metropolitan Government Advanced Research (Grant Number. H31-1).

-
- [1] A. Neubauer, *et al.*, *Physical Review Letters* **102**, 186602 (2009).
 - [2] X. Z. Yu, *et al.*, *Nature* **465**, 901 (2010).
 - [3] T. Schulz, *et al.*, *Nature Physics* **8**, 301 (2012).
 - [4] N. Romming, *et al.*, *Science* **341**, 636 (2013).
 - [5] N. Nagaosa, Y. Tokura, *Nature Nanotechnology* **8**, 899 (2013).
 - [6] S. Mühlbauer, *et al.*, *Science* **323**, 915 (2009).
 - [7] S. Seki, S. Ishiwata, Y. Tokura, *Physical Review B* **86**, 060403 (2012).
 - [8] I. Kézsmárki, *et al.*, *Nature Materials* **14**, 1116 (2015).
 - [9] Y. Tokunaga, *et al.*, *Nature Communications* **6**, 7638 (2015).
 - [10] T. Kurumaji, *et al.*, *Science* **365**, 914 (2018).

- [11] M. Hirschberger, *et al.*, *Nature Communications* **10**, 5831 (2019).
- [12] N. D. Khanh, *et al.*, *Nature Nanotechnology* **15**, 444 (2020).
- [13] S. Ishiwata, *et al.*, *Physical Review B* **101**, 134406 (2020).
- [14] S. Gao, *et al.*, *Nature* **586**, 37 (2020).
- [15] R. Takagi, *et al.*, *Nature Communications* **13**, 1472 (2022).
- [16] Y. Tokura, N. Kanazawa, *Chemical Reviews* **121**, 2857 (2020).
- [17] R. Takashima, H. Ishizuka, L. Balents, *Physical Review B* **94**, 134415 (2016).
- [18] A. Fert, N. Reyren, V. Cros, *Nature Reviews Materials* **2**, 17031 (2017).
- [19] C. Psaroudaki, S. Hoffman, J. Klinovaja, D. Loss, *Physical Review X* **7**, 041045 (2017).
- [20] T. Yokouchi, *et al.*, *Nature* **586**, 232 (2020).
- [21] C. Psaroudaki, C. Panagopoulos, *Physical Review Letters* **127**, 067201 (2021).
- [22] T. Okubo, S. Chung, H. Kawamura, *Physical Review Letters* **108**, 017206 (2012).
- [23] A. O. Leonov, M. Mostovoy, *Nature Communications* **6**, 8275 (2015).
- [24] T. Nomoto, T. Koretsune, R. Arita, *Physical Review Letters* **125**, 117204 (2020).
- [25] D. S. Inosov, *et al.*, *Physical Review Letters* **102**, 046401 (2009).
- [26] Z. Wang, Y. Su, S.-Z. Lin, C. D. Batista, *Physical Review Letters* **124**, 207201 (2020).
- [27] K. Mitsumoto, H. Kawamura, *Physical Review B* **104**, 184432 (2021).
- [28] J. Bouaziz, E. Mendive-Tapia, S. Blügel, J. B. Staunton, *Physical Review Letters* **128**, 157206 (2022).
- [29] R. Ozawa, S. Hayami, Y. Motome, *Physical Review Letters* **118**, 147205 (2017).
- [30] S. Hayami, R. Ozawa, Y. Motome, *Physical Review B* **95**, 224424 (2017).
- [31] S. Hayami, T. Okubo, Y. Motome, *Nature Communications* **12**, 6927 (2021).
- [32] A. Garnier, *et al.*, *Journal of Magnetism and Magnetic Materials* **140–144**, 899 (1995).
- [33] A. Garnier, D. Gignoux, D. Schmitt, T. Shigeoka, *Physica B: Condensed Matter* **222**, 80 (1996).
- [34] T. Samanta, I. Das, S. Banerjee, *Journal of Applied Physics* **104**, 123901 (2008).
- [35] Y. Yasui, *et al.*, *Nature Communications* **11**, 5925 (2020).
- [36] N. D. Khanh, *et al.*, *Advanced Science* **9**, 2105452 (2022).
- [37] S. R. Mishra, *et al.*, *Physical Review Letters* **81**, 1306 (1998).
- [38] R. Ozawa, *et al.*, *Journal of the Physical Society of Japan* **85**, 103703 (2016).

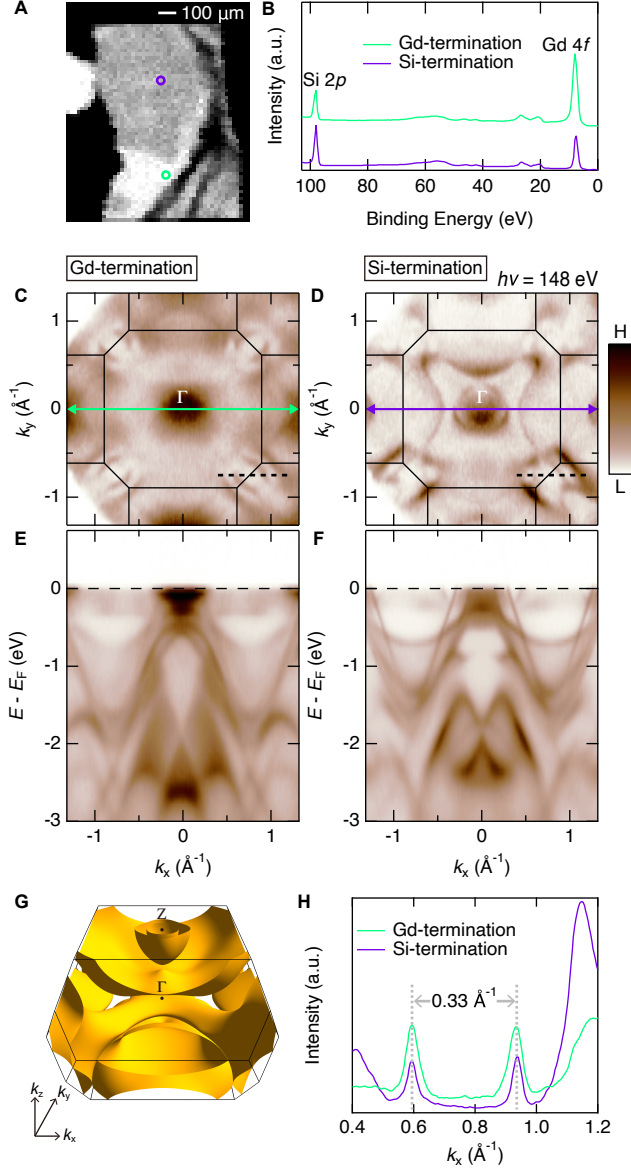


FIG. 1. **Surface terminations of GdRu₂Si₂ and their electronic structures.** (A) Spatial mapping of photoemission intensity around E_F on the cleaved GdRu₂Si₂ surface. The spot size of the synchrotron light is around $40 \times 10 \mu\text{m}^2$. (B) Core level measurements at 2 spots marked by green and purple circles in (A). (C,D) Fermi surface (FS) mappings of Gd-termination (C) and Si-termination (D) measured at 10 K with 148 eV photons corresponding to $k_z = 0$. The solid black lines denote the bulk Brillouin zone (BZ). (E,F) Band dispersion maps of Gd-termination and Si-termination, respectively, measured along momentum cuts crossing the Γ point (green and purple arrows in (C,D)). (G) Calculated FS for the bulk state. (H) Momentum distribution curves (MDCs) along the dashed black lines in (C,D). The dimension arrow represents the peak-to-peak distance, which agrees between the two MDCs.

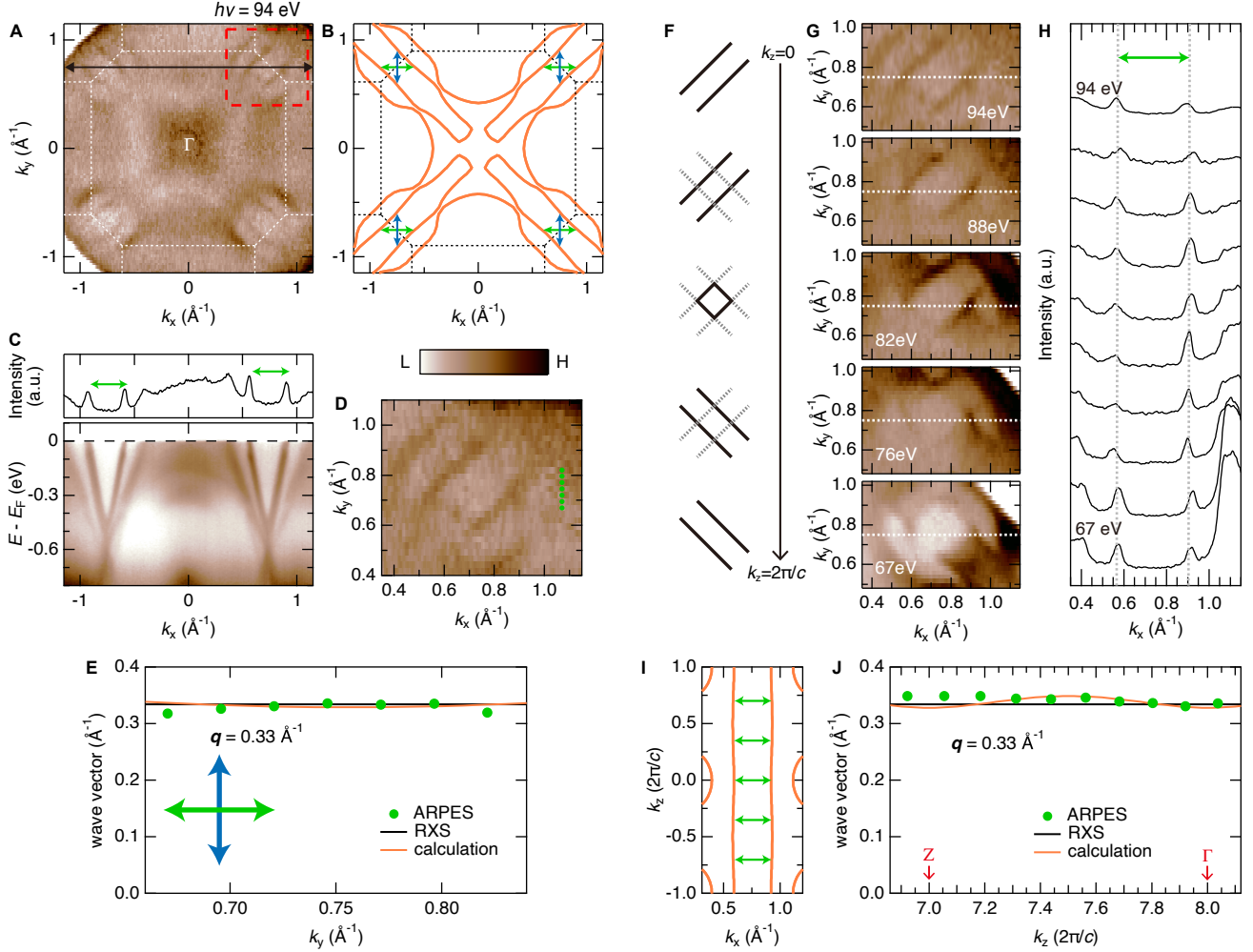


FIG. 2. **Fermi surface nesting in the 3D momentum space.** (A) The Fermi surface (FS) mapping for Gd-termination measured at 10 K with 94 eV photons corresponding to $k_z = 0$. (B) Calculated FS at $k_z = 0$. The dashed white and black lines in (A) and (B), respectively, denote the Brillouin zone (BZ). The green and blue arrows indicate the nesting wave vectors parallel to the k_x and k_y directions, respectively. (C) Band dispersion map connecting the corners of BZ (black arrow in (A)) and the corresponding momentum distribution curve (MDC) at the Fermi level. The length of the nesting wave vector is estimated from the distance between MDC peaks (green arrows). (D) Magnified FS of the red rectangle region in (A). (E) The length of the nesting wave vector along the k_x direction estimated by ARPES (green filled circles) and by calculations (red line), against the k_y positions. The k_y positions for the ARPES results are marked by the green dots in (D). The q -vector length of magnetic modulation reported by the RXS study is also overlaid (black line) in (E). (F, G) Evolution of the nested in-plane FS with changing k_z from 0 to $2\pi/c$, schematically illustrated and demonstrated by ARPES, respectively. The values of k_z are changed from 0 to $2\pi/c$ by sweeping photon energy from 94 eV to 67 eV. (H) MDCs of the nested FS along the white dotted lines in (G), obtained at different photon energies covering k_z s from 0 to $2\pi/c$. The green arrow connects peak to peak in MDC, which corresponds to the length of the nesting wave vector. (I) k_z dependence of the nested part of FS along k_x crossing the BZ corner. (J) The similar plots as in (E), but for the FS nesting along the k_z direction.

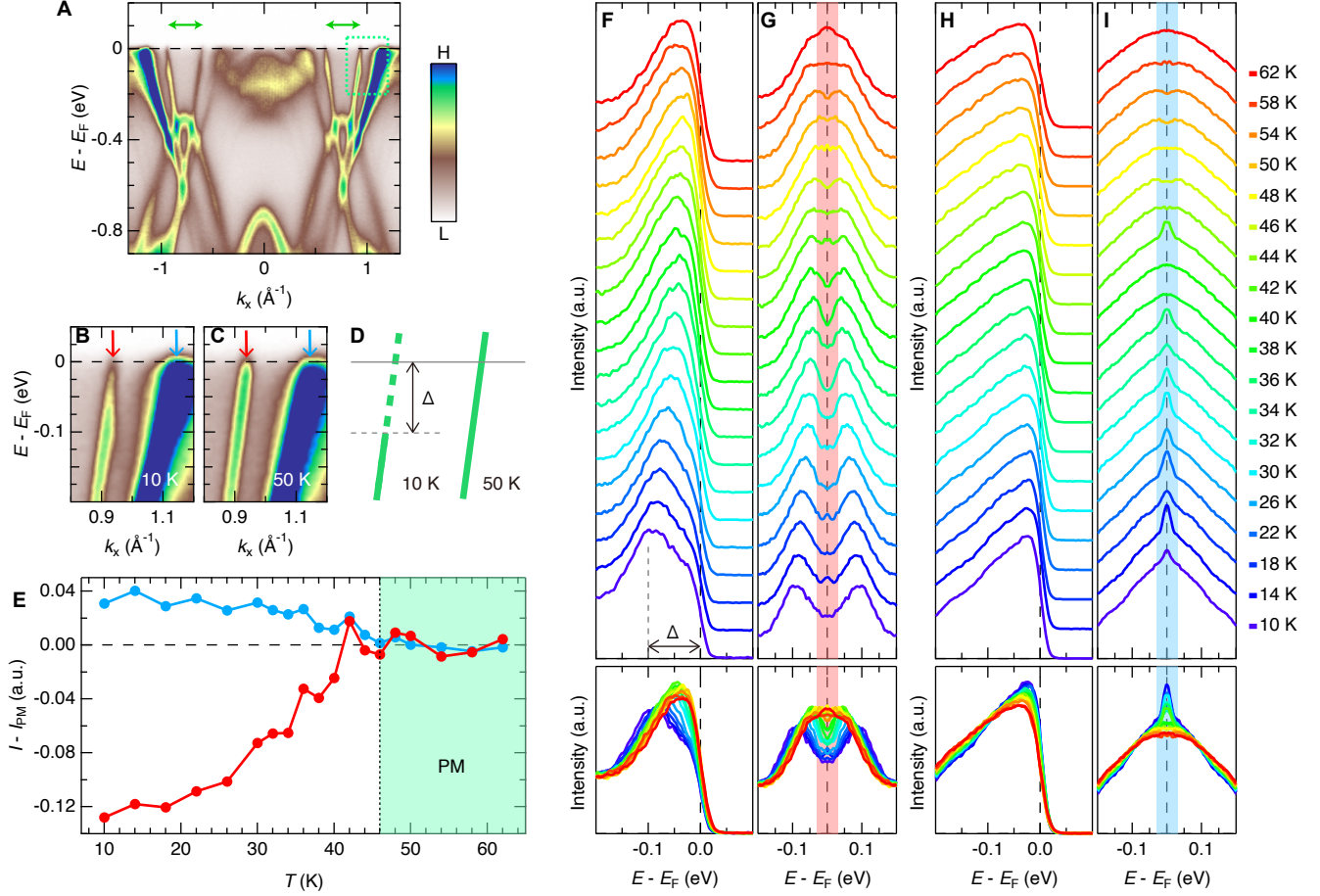


FIG. 3. **The pseudogap at the nested FS and its temperature evolution.** (A) Band dispersion map of Si-termination along a momentum cut connecting the Brillouin zone corners, which capture the nested parts of FS. The used photon energy is 148 eV, corresponding to $k_z = 0$. The green arrows indicate the FS nesting wave vector. (B,C) The magnified image of band dispersions in a green rectangle area of (A) measured below ($T = 10$ K) and above ($T = 50$ K) the magnetic transition temperature ($T_N = 46$ K), respectively. The red and blue arrows point to the nesting and non-nesting bands, respectively. (D) Schematic illustration of the nesting band below and above T_N with and without the pseudogap, respectively. (E) The temperature evolution of spectral weight near E_F for the nesting (red dots) and non-nesting (blue dots) bands, respectively; each is spectral intensity in (G) and (I) integrated within the red and blue hatched region (± 30 meV). (F,H) The energy distribution curves (EDCs) at k_F (red and blue arrows in (B) and (C)) measured at various temperatures for the nesting and non-nesting band, respectively. In the top and bottom panels, the EDCs are plotted with and without an offset, respectively. (G,I) EDCs in (F) and (H), respectively, symmetrized about E_F .

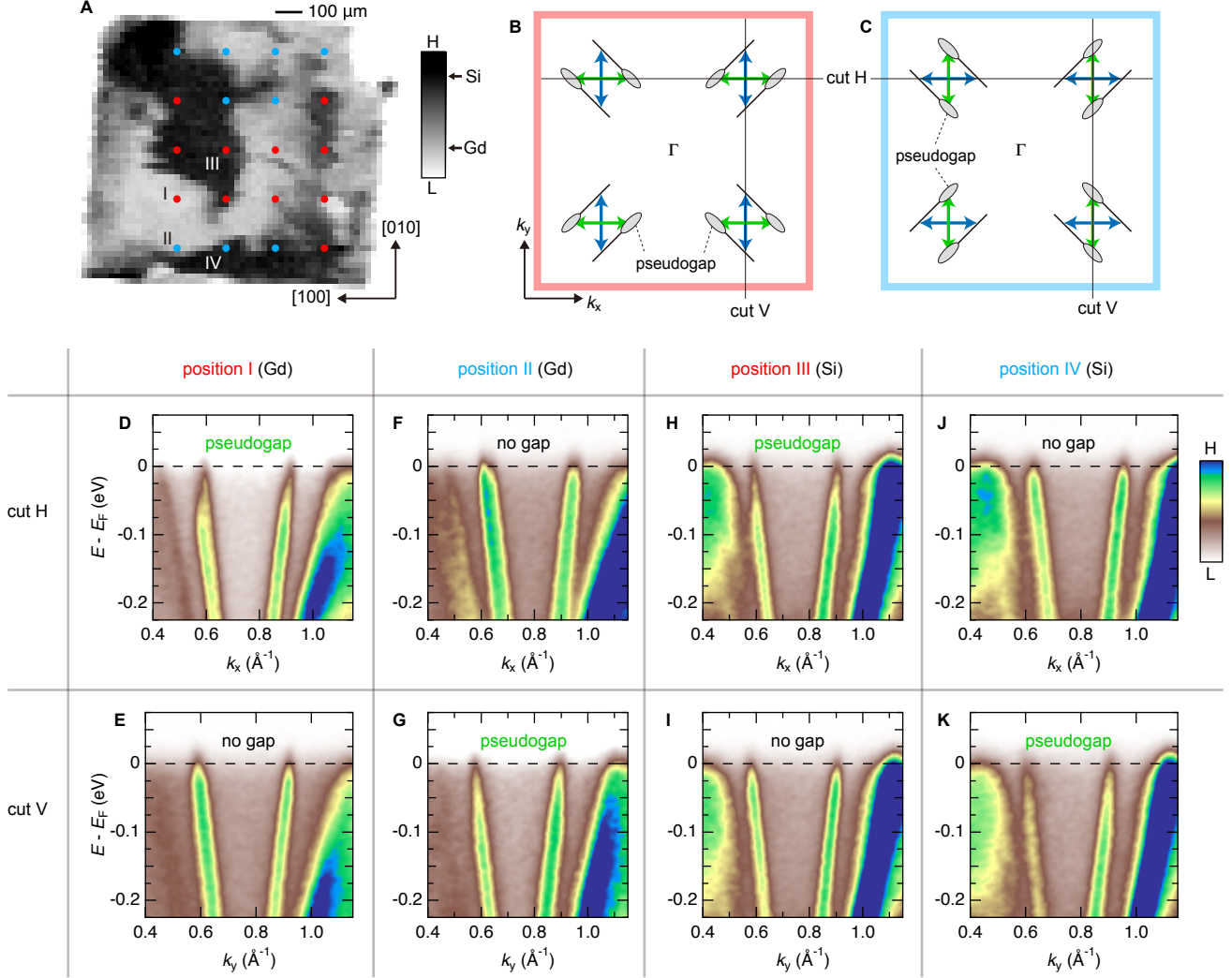


FIG. 4. **Magnetic-domain-dependent pseudogap.** (A) Spatial mapping of photoemission intensity on the GdRu₂Si₂ surface. The black and grey areas (strong and weak intensities) indicate Si-termination and Gd-termination, respectively; note that the correspondence relationship between the color contrast (black and grey) and terminations (Si-termination and Gd-termination) is reversed from that of Fig. 1a since the selected energy-momentum region for photoemission intensity mapping is different (see Supplementary Section II and Fig. S2). Colored dots mark twenty different spots separately measured by ARPES. Red and blue represent two kinds of magnetic domains distinguished by the observation of pseudogap. (B,C) Schematic FS of the two different domains each corresponding to red and blue dot in (A). In the domain of red spots, the pseudogap is observed only along the horizontal cut (cut H). In the domain of blue spots, the pseudogap is observed only along the vertical cut (cut V). (D to K) Band dispersion maps of 4 different spots marked as I, II, III, and IV in (A). Position I and II are from Gd-termination, whereas Position III and IV are from Si-termination. The upper panels (D to J) are obtained along cut H, whereas the lower panels (E to K) are along cut V. Whether or not the pseudogap is observed is described in each panel.

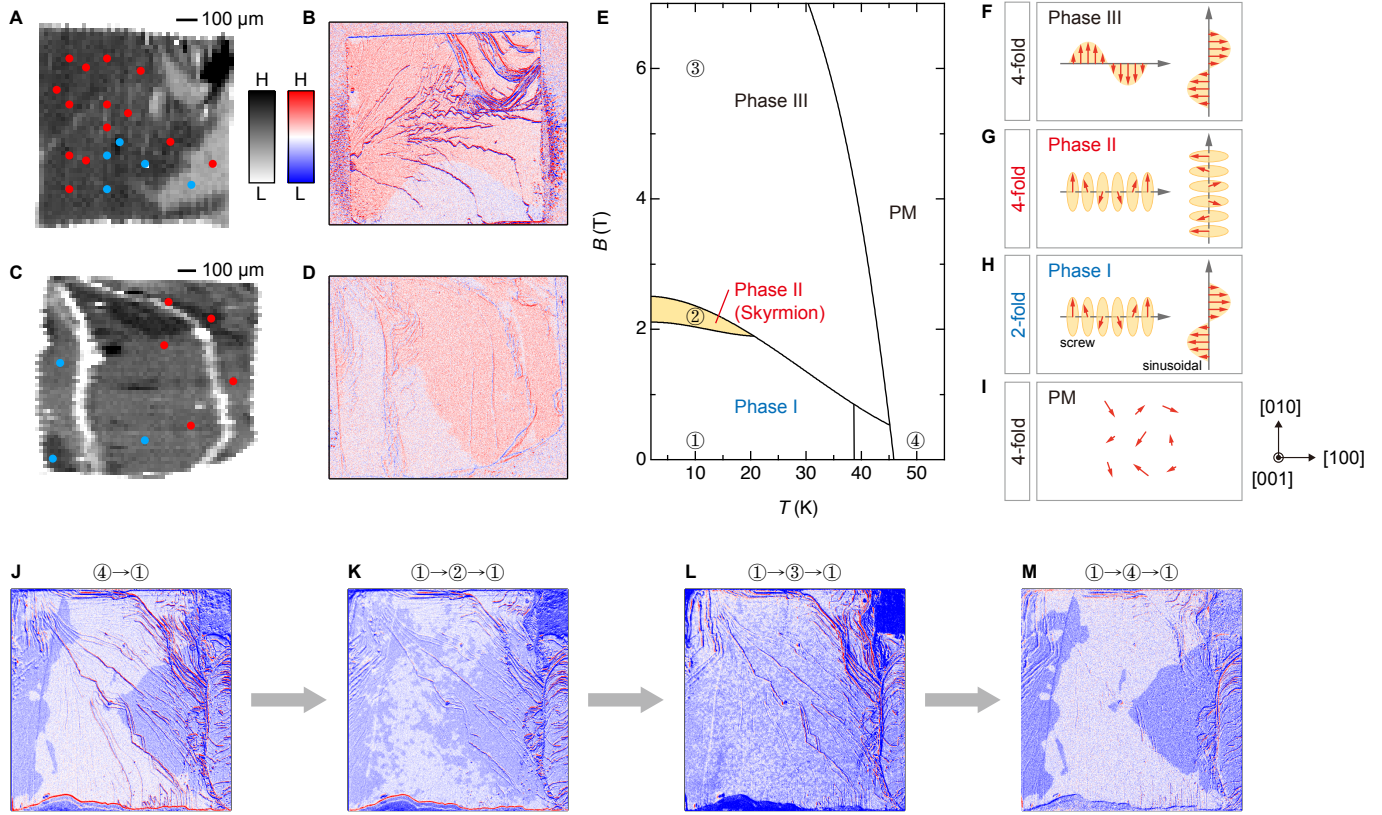


FIG. 5. Manipulation of magnetic domains by field and temperature cyclings. (A,C) Magnetic domains determined by ARPES for sample #1 and sample #2, respectively. Spots separately measured by ARPES are marked on each spatial mapping of photoemission intensity around E_F ; note that the selected momentum region for this intensity mapping differs from that in Fig. 1a. Red and blue colors indicate different magnetic domains distinguished by the different momentum spaces opening the pseudogap. (B,D) Magnetic domains visualized by polarizing microscopy. The image plots the intensity difference below and above the Néel temperature (10 K and 50 K), displaying two kinds of magnetic domains (red and blue areas). (E) Magnetic phase diagram of GdRu_2Si_2 [12]. (F to I) Schematics of spin texture for Phase III, Phase II, Phase I, and paramagnetic (PM) phase, respectively [36]. Only Phase I has a 2-fold magnetic structure. (J to M), Magnetic domains observed by polarizing microscopy after different procedures of temperature and field cyclings: Cooling down from 50 K to 10 K (J). Excited to Phase II and come back to Phase I (K). Excited to Phase III and come back to Phase I (L). Temperature cycling from 10 K to 50 K and back to 10 K (M). For the field cycling, a pulsed magnetic field is used. All images are measured at 10 K without field and subtracted by the image of the PM phase at 50 K.

Supplementary Materials for
Magnetic-domain-dependent pseudogap induced by Fermi surface
nesting in a centrosymmetric skyrmion magnet

arXiv:2307.08000v1 [cond-mat.mtrl-sci] 16 Jul 2023

Materials and methods

Samples:

High quality single crystals of GdRu_2Si_2 were grown by the Czochralski pulling method using a tetra-arc furnace in an argon atmosphere. The starting materials were 3N(99.9% pure)-Gd, 3N5-Ru and 6N-Si. The obtained single crystals were oriented by X-ray Laue diffraction, and cut into rectangular shapes by spark cutting. The typical size of these crystals was $1.0 \times 1.0 \times 0.6 \text{ mm}^3$.

ARPES:

The synchrotron-based ARPES was performed at beamline 5-2 of Stanford Synchrotron Radiation Lightsource (SSRL) with photon energies ranging from 60 eV to 200 eV. The spot size of the light is around 40 (horizontal) \times 10 (vertical) μm^2 . With the ScientaOmicron DA30L analyzer, FS mapping can be conducted over momentum space covering the entire BZ without sample rotation. The spatial photoemission mapping is measured by moving the manipulator with a step of 20 μm . The light polarization was set to linear horizontal (perpendicular to the analyzer slit) during the measurement. The overall angular resolution is better than 0.2° and the energy resolution is around 20 meV. The samples were cleaved *in situ* at the measurement temperature of 10 K with the chamber pressure lower than 4×10^{-11} torr.

DFT calculations:

The DFT calculations were performed using the Perdew-Burke-Ernzerhof parametrization of the generalized gradient approximation [1] and the projector augmented wave (PAW) method [2] as implemented in the Vienna *ab initio* simulation package [3–6]. We used lattice parameters of $a = b = 4.1634 \text{ \AA}$ and $c = 9.6102 \text{ \AA}$ taken from Ref. [7] and atomic coordinates optimized in calculation. The core electrons in the PAW potentials were $[\text{Kr}]5s^2 5d^{10} 4f^7$ for Gd, $[\text{Kr}]$ for Ru, and $[\text{Ne}]$ for Si, where $4f^7$ occupation for Gd^{3+} was handled with open-core treatment. The plane-wave cutoff energy of 320 eV and a $10 \times 10 \times 10$ k -mesh were used with the inclusion of the spin-orbit coupling.

We constructed Wannier functions [8, 9] of Gd- d , Ru- d , and Si- sp orbitals from the calculated band dispersion using the Wannier90 software [10]. The outer and inner energy windows for Wannierization were $[-11:12] \text{ eV}$ and $[-11:1] \text{ eV}$, respectively, where the Fermi energy was set to zero. A $16 \times 16 \times 16$ k -mesh was used for Wannierization. The tight-binding model consisting of these Wannier functions was used for calculating FS. Two- and three-dimensional FS were calculated using 100×100 and $100 \times 100 \times 100$ k -meshes, respectively. We used the FermiSurfer software [11] for depicting three-dimensional FS.

Polarizing microscopy measurement:

The polarizing microscopy was performed at the Institute for Solid State Physics, the University of Tokyo. For details of the apparatus, see Ref. [12]. The (001) plane was observed; the same sample surface measured by ARPES was observed just after the ARPES experiment. In the polarizing microscopy measurement, the analyzer was set 3 degrees from the crossed Nicole configuration. Pulsed fields of 4.6 ms duration normal to the plane of observation were applied using a nondestructive pulse magnet. The sample temperature was controlled in the range of 10-60 K by thermal conduction from a cryocooler.

Section I: Determination of surface terminations for Fig. 1A

To determine the terminations for the cleavage surface of GdRu_2Si_2 , we scanned the sample surface by vacuum ultraviolet light with a spot size of $40 \times 10 \mu\text{m}^2$. By selecting different energies for photoemission detection by the analyzer, we can get different contrasts of spatial mappings, although the obtained termination patterns are the same. Figure S1A (same data as Fig. 1A) displays the intensity map of photoemission signals near E_F (143.5 eV) for the ARPES band dispersion across the Γ point, obtained by the incident light of 148 eV. The white part represents a higher local density of states (LDOS) than the brown part. According to the previous STM measurements, there are only two kinds of terminations (Gd-termination and Si-termination), and Gd-termination has a higher LDOS near E_F than Si-termination [13]. This suggests that the white part is Gd-termination and the brown part is Si-termination. To confirm this, we set the energy range to the binding energy of Si $2p$ in the photoelectron detection and obtained the spatial mapping in Fig. S1B. Since Si-termination should have a stronger signal than Gd-termination, the white part is Si-termination and the brown part is Gd-termination. Although the relationship between high and low intensities is reversed, the termination patterns are consistent between the two different mappings of Fig. S1A and Fig. S1B.

Section II: Determination of surface terminations for Fig. 4A

As mentioned above, we used the ARPES signal of a band dispersion across the Γ point and near E_F for spatial intensity mapping for Fig. 1A. Here, we demonstrate that termination patterns can be even more clearly visualized (as presented in Fig. 4A) if a band dispersion in a different momentum-energy region is selected for spatial intensity mapping.

Figure S2A,B shows the Fermi surface (FS) of GdRu_2Si_2 for Gd-termination and Si-termination, respectively (same figures as Fig. 1C,D). Now we focus on the ARPES band dispersions along the nesting FS (green and purple arrow in Fig. S2A,B), as shown in Fig. S2C,D. An apparent difference between these two ARPES dispersions is that only Si-termination exhibits a band dispersion around -0.8 eV within a red rectangle. The

spatial intensity mapping of this energy-momentum region is displayed in Fig. S2E. The color contrast is high, clearly visualizing patterns of Si-termination (black, strong intensity) and Gd-termination (grey, weak intensity) on the surface. Note that the correspondence relationship between intensities and the two domains is reversed from that of Fig. 1A (or Fig. S1A); in Fig. 1A, Si-termination corresponds to weak intensity, and Gd-termination to strong intensity.

Section III: Calculated Fermi surface at different k_z values

Figure S3A shows the calculated 3D Fermi surface (FS) in the first Brillouin zone (BZ). In Fig. S3B,C, we show the cross-sections of the FS across the Γ point ($k_z = 0$) and the Z point ($k_z = 2\pi/c$), respectively. The nesting part of the FS is located at the corner of the BZ, as marked by the green square. As is clear by comparing the green square regions zoomed in Fig. S3D,E, the nested part of FS is rotated by 90° when k_z is changed from 0 to $2\pi/c$.

Section IV: The temperature dependence of resistivity in GdRu_2Si_2

We measured the resistivity of GdRu_2Si_2 at a zero magnetic field after ARPES experiments (Fig. S4). Importantly, an upturn is seen around 46 K (pointed by an up-arrow), as previously reported [14]. This is compatible with our ARPES observation that the pseudogap opens in the electronic structure upon cooling below the transition temperature from the paramagnetic to magnetic phase. In the resistivity behavior, we also found a small kink near 39 K (pointed by a down-arrow) corresponding to the second transition temperature below which GdRu_2Si_2 enters Phase I.

Section V: Magnetic-domain-dependent pseudogap revealed by ARPES

During ARPES measurements at many spots on the GdRu_2Si_2 surface, we discovered that the pseudogap is opened in the parallel parts of FS at some spots, whereas it is absent at other spots, although measuring the same momentum region. This suggests that the pseudogap has domain dependence. To fully understand this, we have thoroughly investigated the relationship between the real space positions and the momentum positions where the pseudogap is opened. For real space mapping, the beam spot of the incident light needs to be scanned on the sample surface. For a fair comparison of magnetic domains in ARPES, one needs to observe the different domains at the same experimental geometry about the direction of the incident light, the light polarization, and the analyzer slit direction; this can avoid confusion coming from the matrix element effect in ARPES. These experimental

requirements are hard to be fulfilled since magnetic structures of different domains are mutually rotated by 90° on the same sample surface. We overcome the difficulty by ARPES measurements combined with the in-situ in-plane rotation of samples and the spatial scan of the synchrotron beam on the sample surface, as demonstrated in Fig. S5, by making the most use of the high-precision sample manipulator.

In the experimental geometry of Fig. S5A, the slit direction of an ARPES analyzer is along the sample axis marked by the red line. This setting allows observing the band dispersion of cut H (along k_x), as illustrated in Fig. S5B together with the parallel parts of FS. By rotating the sample by 90° around the z -axis, the analyzer slit becomes perpendicular to the red sample axis (Fig. S5D), so the observable band dispersion is changed to cut V (along k_y), as drawn in Fig. S5E. The advantage of this experimental procedure is that we can measure the band dispersions along cut H and cut V at the same experimental geometry (the direction of the incident light, the light polarization, and the analyzer slit direction) and can compare magnetic domains at the same condition. This experiment, however, needs to be combined with a spatial mapping technique of the surface to follow the same spot for ARPES measurement after the 90° rotation of samples.

In Fig. S5G, the spots measured along cut H by ARPES are marked on the photoemission intensity map distinguishing Si-termination (black color) and Gd-termination (grey color) on the surface. We found that the pseudogap is opened in the band dispersion measured at the green dots, while it is absent at the orange dots. After 90° rotation of the sample (Fig. S5H), we measured the same spots by ARPES, but along cut V in this case. Again, green and orange represent that the pseudogap is opened and absent, respectively. Interestingly, we found that the green dots turned to orange dots, and inversely, the orange dots turned to green dots after the sample rotation. This indicates that there are two kinds of magnetic domains; one kind opens the pseudogap only along cut H, whereas the other kind opens it only along cut V.

Figure S5C,F presents a typical set of band dispersions measured along cut H and cut V, respectively, from the same spot (arrow in Fig. S5G and S5H). We find that the pseudogap is observed along cut H, whereas it is not along cut V. These data indicate that the electronic structure of each domain has the 2-fold symmetry in GdRu_2Si_2 .

Section VI: Correspondence between polarizing microscope images and ARPES results.

The polarizing microscope is a common measure to distinguish the magnetic domains of GdRu_2Si_2 . Two kinds of magnetic domains are expected to emerge in Phase I because of the 2-fold symmetry in the magnetic order. The optical birefringence visualizing such

domain patterns is indeed observed in Phase I (Fig. S6A, measured at 10 K). In contrast, polarizing microscope intensities become homogeneous over the sample surface in the PM phase (Fig. S6B, measured at 60 K). The patterns of magnetic domains in Phase I become clearer with better contrast (Fig. S6C) when the image at 10 K (Phase I) is subtracted by that at 60 K (PM phase). In the following experiments, therefore, the image of the PM phase is always subtracted from that of the magnetic order phases for clearer visualization of magnetic domain patterns.

Next, we compare the polarizing microscope image with the ARPES data. Figure S6D shows that eight measurement spots are categorized into two different domains. At blue spots, the pseudogap is absent along cut H (see Fig. S5B), as demonstrated in Fig. S6E,F. In contrast, the red spots open the pseudogap in the nesting band along cut H, exhibiting a pen-point shape near E_F due to a spectral weight loss (Fig. S6G-I). Importantly, the regions of blue and red dots determined by ARPES (Fig. S6D) perfectly match the magnetic domains (blue and red regions) observed by a polarizing microscope (Fig. S6C). This clarifies that the different magnetic domains in Phase I open the pseudogap in different parts of the nesting FS: one is along cut H and the other along cut V.

Section VII: Evolution of magnetic domains with pulsed field and temperature

In GdRu_2Si_2 , magnetic domains exist only in Phase I, since only Phase I develop a magnetic structure of the 2-fold symmetry, whereas the other phases remain 4-fold symmetry. The magnetic domain patterns could change whenever the phase transition occurs from the other phases (4-fold symmetry) to Phase I (2-fold symmetry). We investigate the evolution of magnetic domains with a polarizing microscope by the magnetic field and temperature cyclings. Here, a pulsed magnetic field with a time width of 4.6 ms is used for the field cycling.

In Fig. S7A, we confirm magnetic domains appearing by decreasing temperature from 50 K (PM phase) to 10 K (Phase I). There are clear boundaries between white and blue domains. By applying a 2.4 T pulsed magnetic field, the system is excited to Phase II (skyrmion phase) and then back to Phase I. Figure S7B1-B4 displays the distributions of magnetic domains changing after sequentially applying a 2.4 T pulsed field 1 time, 5 times, 10 times, and 20 times, respectively. We find that small bubbles of magnetic domains emerge near the original domain boundaries (Fig. S7B1). As increasing the number of times to apply the pulsed field, more magnetic domain bubbles appear. Interestingly, the bubbles always appear near the magnetic domain boundaries, and the body center of the original domains (white and blue large areas) remains unchanged. There is also the tendency that the blue domain gradually gets larger when we repeat applying a magnetic field. However,

the growth speed of the blue domain eventually becomes slower after 10 times of applying a pulsed field, and then the blue domain size almost saturates after 20 times.

After all of these processes, we then applied a pulsed field of 6 T which excite the system to Phase III before coming back to Phase I within 4.6 ms. Figure S7C1,C2 display the resulting distributions of the magnetic domains after applying the field 1 time and 5 times, respectively. We found that the large domains (white and blue areas) break into many small bubbles, which are distributed completely randomly all over the sample after 1-time shot of the pulsed magnetic field. It does not change by repeating the pulse shots. There are two main differences from the experiments with a 2.4 T pulsed magnetic field (Fig. S7B1-B4). One is that the change of domain distribution is utterly random, not occurring only near the boundaries. The second is that there is no preference for one particular domain (like the blue area) growing with applying magnetic fields.

Finally, we heated up the sample from 10 K (Phase I) to 50 K (PM phase) and then cooled it down to 10 K (Phase I). Figure S7D1-D4 displays the domain distributions after that temperature cycle (10 K - 50 K - 10 K) 1 time, 2 times, 3 times, and 4 times, respectively. Note that they were measured just after the domain pattern got completely random with many bubbles by a pulsed magnetic field. Intriguingly, we found that the magnetic domain pattern is perfectly restored to the original one (Fig. S7A).

The series of our experiments in Fig. S7 manifest the capability of magnetism of GdRu_2Si_2 that the memorized pattern of magnetic domains in Phase I can be erased or restored by selectively applying magnetic field cycling or temperature cycling.

Section VIII: Evolution of magnetic domains with static magnetic fields

Here, we demonstrate that magnetic domain bubbles appear also with static magnetic fields, not only with a pulsed field as presented in the main paper and the previous section. For this purpose, we use different equipment utilizing a physical property measurement system (PPMS; PPMS-14T, Quantum Design), which allows setting samples under a static magnetic field. The polarizing microscope images were taken through an infinity-corrected objective lens inserted into the sample space by the microscope which is set above the PPMS at approximately 1 m from the sample position (see Ref. [15] for the details of the apparatus). For comparison, we took the magnetic domain image with both this equipment and the one used in the previous section from the same sample surface, as displayed in Fig. S8C and Fig. S8A, respectively. In the PPMS setup (Fig. S8C), the relatively long distance of 1 m from the sample to the microscope results in a narrower field of view than in the previous experimental configuration (Fig. S8A). Nonetheless, we could confirm the same crack and domain boundary on the surface.

Figure S8B shows the phase diagram of GdRu_2Si_2 , in which the sequence of measurements we performed is indicated by arrows. The polarizing microscope images obtained are displayed from Fig. S8A to Fig. S8K. The red and blue arrows depicted here represent the sequence order of measurements and correspond to those indicated in Fig. S8B. All the images are subtracted in intensity by that obtained at 60 K and 0 T (PM phase) to enhance the color contrast of magnetic domains. On the top of each Fig. S8A-K, the experimental conditions are described.

When cooling from the PM phase to Phase I (grey arrow in Fig. S8B), a sharp domain boundary appears, as pointed by the arrow in Fig. S8C. The domain boundary is unchanged even if a magnetic field of 1 T is applied (Fig. S8D). This indicates that domain distributions remain the same as long as the system is in Phase I. A change occurs when it leaves Phase I, as demonstrated in Fig. S8E-I. The magnetic domain boundary disappears when the static field gets larger than 2.3 T and makes the system enter Phase II (skyrmion phase) and Phase III. When the static magnetic field is decreased (Fig. S8I,H) and the system enters Phase I again (Fig. S8J), the domain bubbles appear near the original domain boundary. The pattern of domain bubbles remains the same even when the static magnetic field is reduced to 0 T (Fig. S8K).

The magnetic domain distributions change only when the system crosses the phase border between Phase I and Phase II. To clarify this, we plot the difference image of Fig. S8D (Phase I) and Fig. S8E (Phase II) in Fig. S8L, and that of Fig. S8J (Phase II) and Fig. S8J (Phase I) in Fig. S8M. These images clearly demonstrate that the original domain boundary disappears when crossing the phase border by increasing the static magnetic field, and small domain bubbles appear when crossing the phase border by decreasing the static magnetic field.

-
- [1] J. P. Perdew, K. Burke, M. Ernzerhof, *Physical Review Letters* **77**, 3865 (1996).
 - [2] G. Kresse, D. Joubert, *Physical Review B* **59**, 1758 (1999).
 - [3] G. Kresse, J. Hafner, *Physical Review B* **47**, 558 (1993).
 - [4] G. Kresse, J. Hafner, *Physical Review B* **49**, 14251 (1994).
 - [5] G. Kresse, J. Furthmüller, *Computational Materials Science* **6**, 15 (1996).
 - [6] G. Kresse, J. Furthmüller, *Physical Review B* **54**, 11169 (1996).
 - [7] K. Hiebl, C. Horvath, P. Rogl, M. J. Sienko, *Journal of Magnetism and Magnetic Materials* **37**, 287 (1983).
 - [8] N. Marzari, D. Vanderbilt, *Physical Review B* **56**, 12847 (1997).
 - [9] I. Souza, N. Marzari, D. Vanderbilt, *Physical Review B* **65**, 035109 (2001).

- [10] G. Pizzi, *et al.*, *Journal of Physics: Condensed Matter* **32**, 165902 (2020).
- [11] M. Kawamura, *Computer Physics Communications* **239**, 197 (2019).
- [12] I. Katakura, *et al.*, *Review of Scientific Instruments* **81**, 043701 (2010).
- [13] Y. Yasui, *et al.*, *Nature Communications* **11**, 5925 (2020).
- [14] T. Samanta, I. Das, S. Banerjee, *Journal of Applied Physics* **104**, 123901 (2008).
- [15] Y. Kinoshita, T. Miyakawa, X. Xu, M. Tokunaga, *Review of Scientific Instruments* **93**, 073702 (2022).

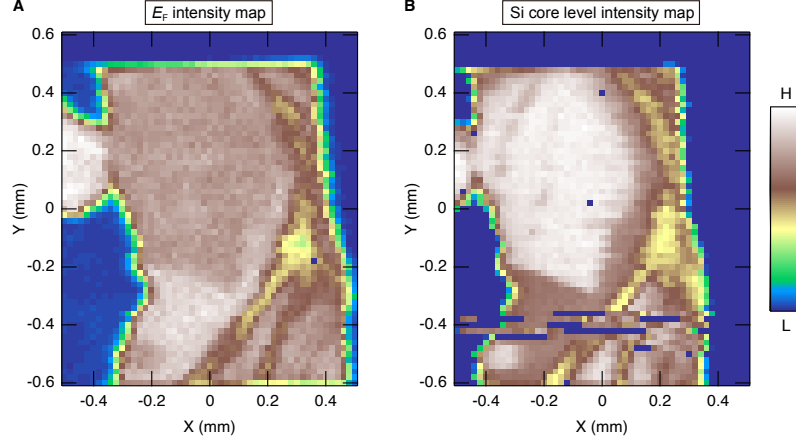


Fig. S1. **Determination of surface terminations for Fig. 1A.** (A) Spatial mapping of photoemission intensities near E_F of ARPES dispersion crossing the Γ point. Here, we use 148 eV photons for incident light and measure photoemission intensities near 143.5 eV. (B) Spatial mapping of photoemission intensities for the Si $2p$ peak around 48 eV.

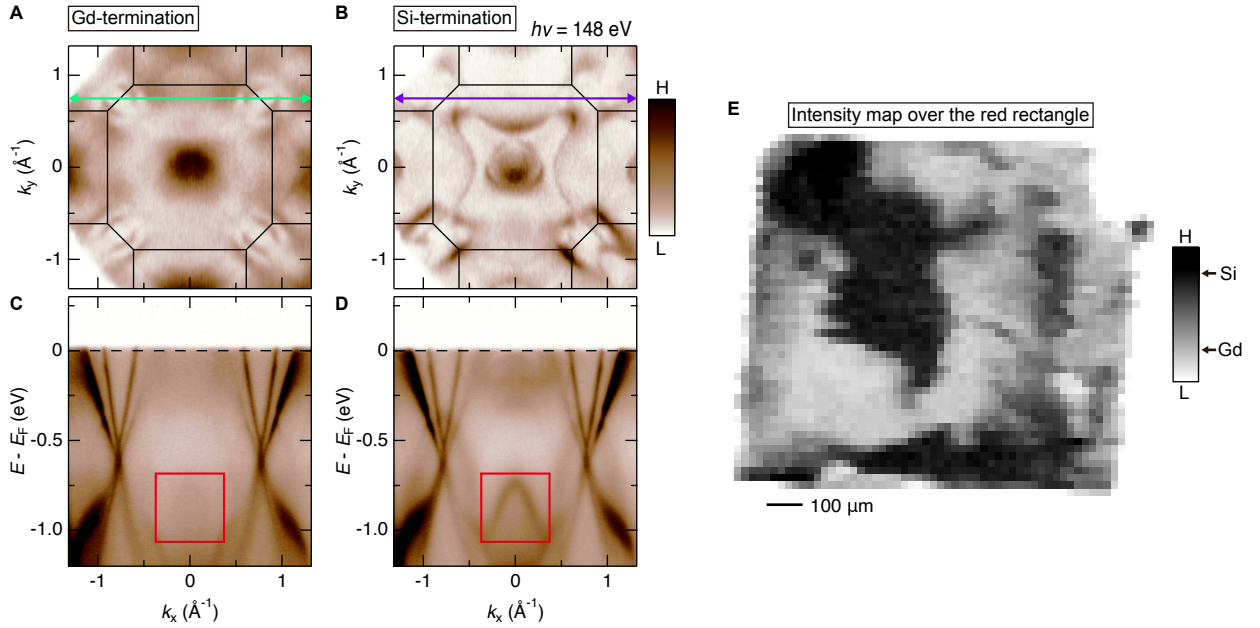


Fig. S2. **Determination of surface terminations for Fig. 4A.** (A,B) Fermi surface (FS) mappings of Gd-termination (A) and Si-termination (B) measured at 10 K with 148 eV photons corresponding to $k_z = 0$ (same figures as Fig. 1C,D). (C,D), Band dispersion maps of Gd-termination and Si-termination, measured along the nesting FS (green and purple arrows in ((A) and (B), respectively). (E) Spatial mapping of photoemission intensities integrated within the red rectangle in (C) and (D) (same figure as Fig. 4A). Black and grey areas (strong and weak intensities) indicate Si-termination and Gd-termination, respectively. Note that the correspondence relationship between the strong-weak contrast and two terminations is reversed from that of Fig. 1A (or Fig. S1A).

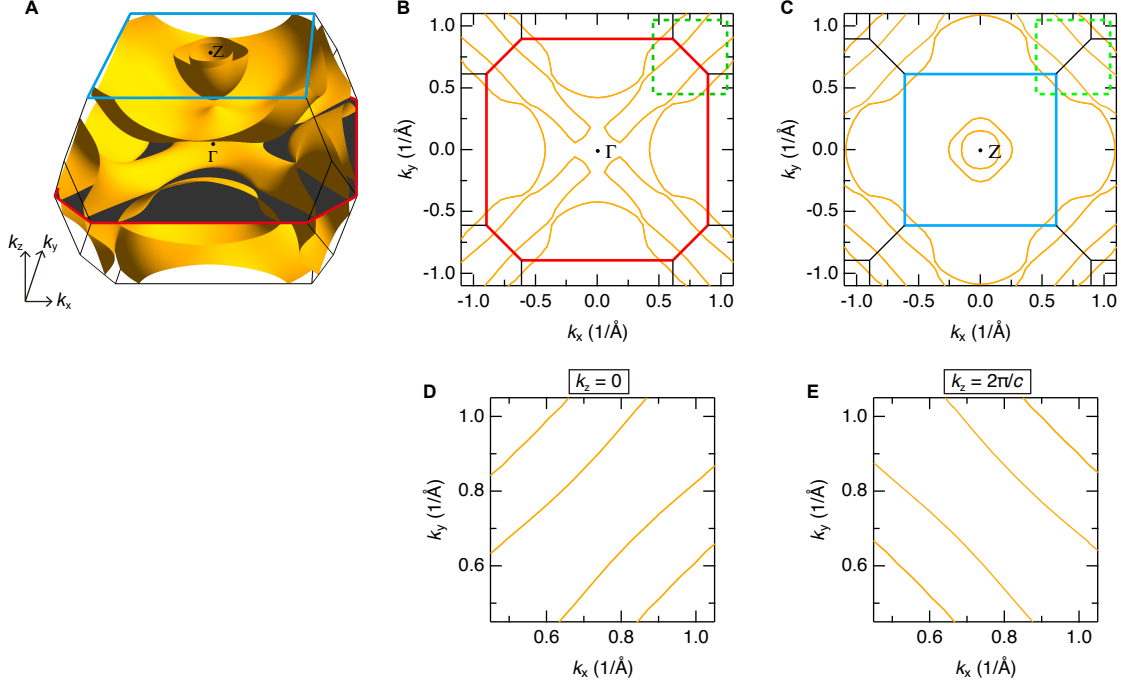


Fig. S3. **Calculated Fermi surface at different k_z values.** (A) 3D Fermi surface (FS) in the first Brillouin zone (BZ). (B) FS at $k_z = 0$ across the Γ point. Red lines indicate the first BZ at $k_z = 0$. (C) FS at $k_z = 2\pi/c$ across the Z point. Blue lines indicate the first BZ at $k_z = 2\pi/c$. (D, E) Magnified FS for the nesting part at the same k_x - k_y region marked by the green square in ((B) $k_z = 0$) and ((C) $k_z = 2\pi/c$), respectively.

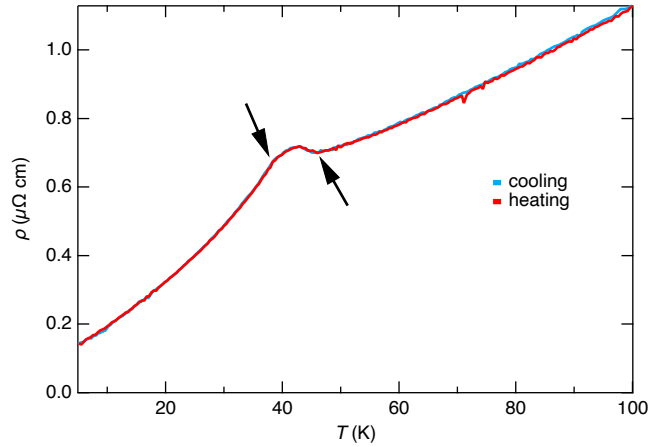


Fig. S4. **The temperature dependence of resistivity in GdRu_2Si_2 .** The resistivity is measured upon both cooling and heating; these two show perfect matching. The up arrow around 46 K marks the onset of an upturn behavior, and the down arrow around 39 K marks a kink behavior, respectively.

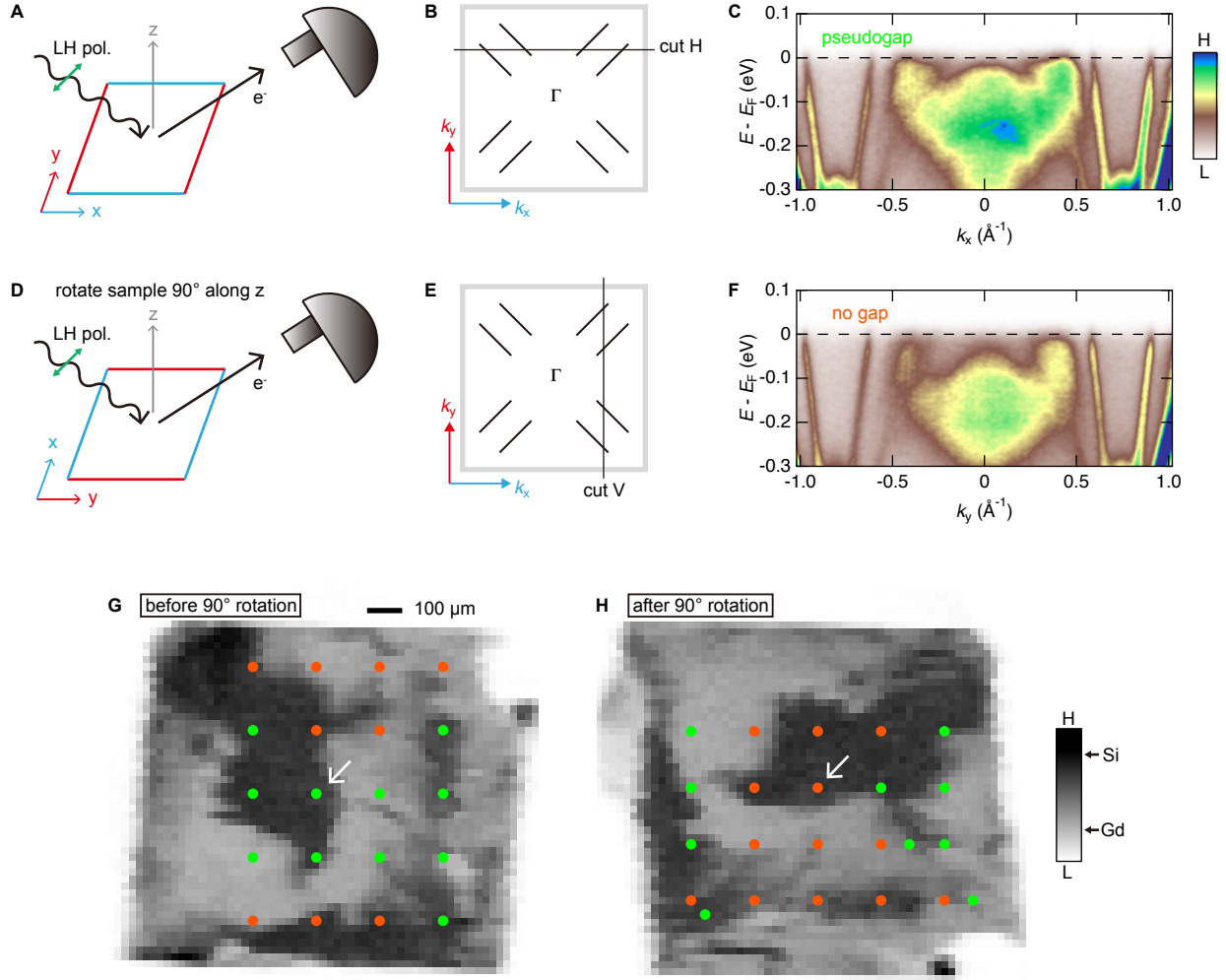


Fig. S5. **Magnetic-domain-dependent pseudogap revealed by ARPES.** (A,D) Schematic of experimental geometry before (A) and after (D) rotating sample by 90° along the z-axis. (B,E) Illustrations of two momentum cuts along k_x (cut H) and k_y (cut V) crossing the nested parts of the Fermi surface, which can be measured before and after the sample rotation (A and D), respectively. (C,F) ARPES band dispersions measured at the same spot on the surface (arrows in (G) and (H)) before and after the sample rotation (A and D), respectively. The pseudogap is opened along cut H measured before the sample rotation, while there is no gap along cut V measured after the rotation. (G,H) Measured spots (green and orange dots) marked on the spatial mapping of photoemission intensities before and after rotation, respectively. The black and grey regions in the intensity map correspond to Si-termination and Gd-termination, respectively. In (G), the green dots represent the spots where the band dispersion along cut H (along k_x , as in (B)) shows the pseudogap, whereas the orange dots represent where the gap is absent. In (H), the green and orange dots represent the spots where the pseudogap is opened and absent, respectively; note, however, the measurement is now along cut V (along k_y , as in (E)), differently from the case in (G). The white arrows in (G) and (H) mark the same spot before and after the sample rotation, which is measured in (C) and (F) along cut H and cut V, respectively.

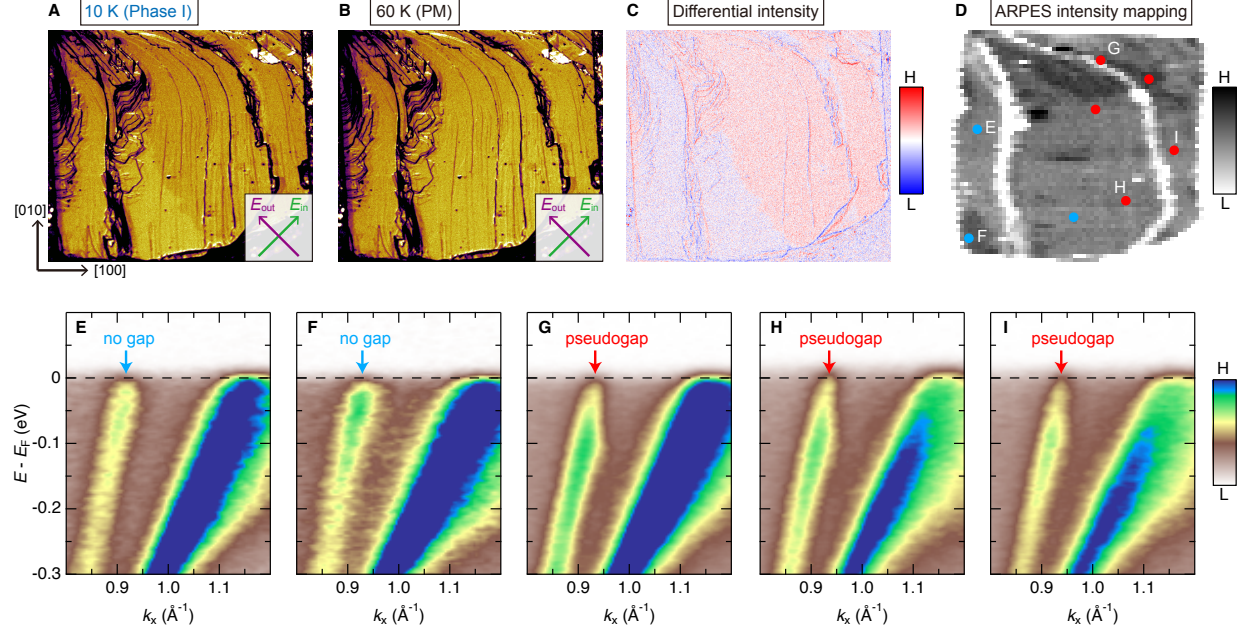


Fig. S6. Correspondence between polarizing microscope images and ARPES results. (A) Polarizing microscope image of the GdRu_2Si_2 surface at 10 K (Phase I). The inset shows the relative direction of the incident and outgoing light with respect to crystal axes in polarizing microscope imaging. (B) Polarizing microscope image at 60 K (PM phase). (C) Difference intensity map between (A) and (B) visualizing two kinds of magnetic domains (red and blue areas). (D) Photoemission intensity map for the same sample surface as observed by polarizing microscope in (C). The dots on the image mark spots measured along cut H (see S5b) by ARPES. Red and blue indicate that the pseudogap is opened and absent in the parallel parts of the Fermi surface, revealing that there are two magnetic domains, consistent with the image in (C). (E to I) Band dispersions measured along cut H at different spots on the sample surface (dots in (D)), focusing on whether the pseudogap is opened or absent (marked by arrows). Alphabets labeled for dots in (D) correspond to alphabets for the panel names.

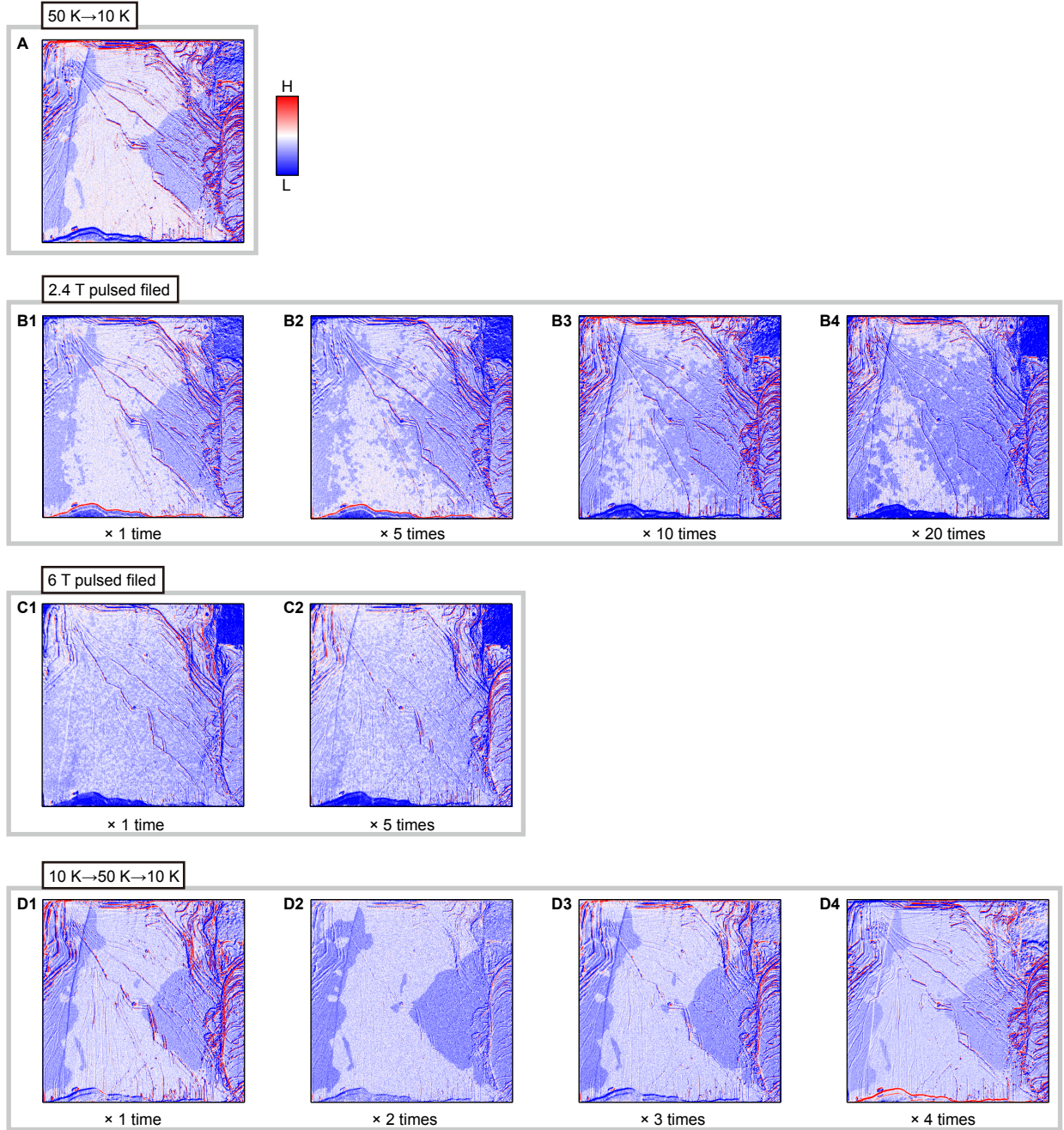


Fig. S7. **Evolution of magnetic domains with pulsed field and temperature.** Polarizing microscope images after cooling down from 50 K (PM phase) to 10 K (Phase I) without a magnetic field (A), applying pulsed magnetic field to excite the system to Phase II and then back to Phase I several times (B1 to B4), applying pulsed magnetic field to excite the system to Phase III and then back to Phase I several times (C1,C2), and heating from 10 K (Phase I) to 50 K (PM phase) and then cooling back to 10 K (Phase I) several times (D1 to D4). All images are measured at 10 K (Phase I), and they are subtracted by the images at 50 K (PM phase) for the purpose of background subtraction.

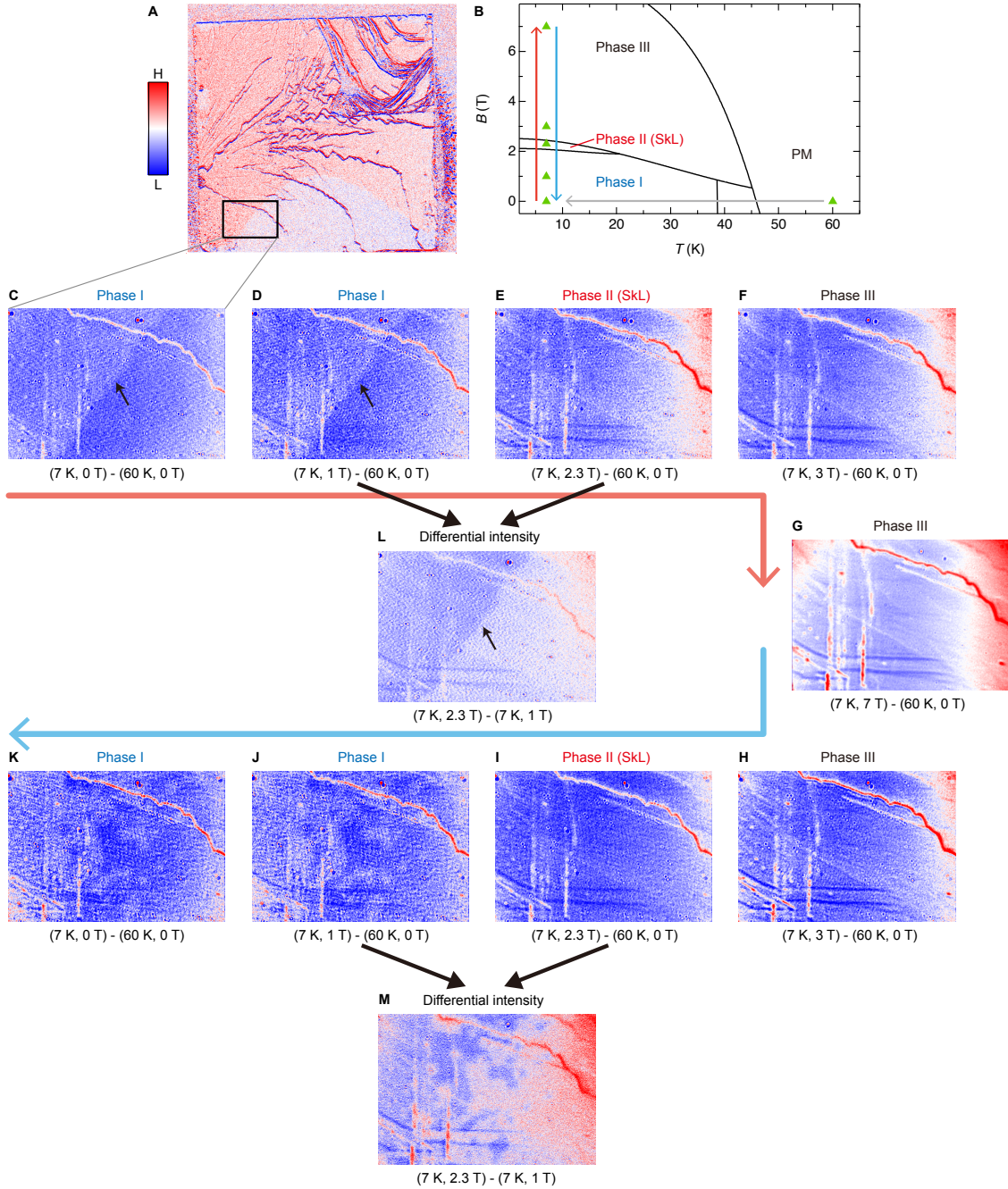


Fig. S8. **Evolution of magnetic domains with static magnetic fields.** (A) Polarizing microscope image in Phase I measured over a wide view. The black rectangle marks the observed region for polarizing microscope images in (C to K) with the apparatus of the PPMS setup. (B) Phase diagram of $GdRu_2Si_2$. The green triangles mark the temperature and static field conditions of the measurements. The red and blue arrows represent the measurement sequence; the red and blue arrows connecting panels (C to K) also correspond to these arrows. (C to K) Polarizing microscope images exhibiting magnetic domain distribution at different Phases. They are subtracted by the image at 60 K (PM phase) for better contrast. Measurement conditions are described at the bottom of each panel. Arrows in (C,D) indicate the domain boundary. (L) Difference intensities between two images of ((D) Phase I) and ((E) Phase II). (M) Difference intensities between two images of ((J) Phase I) and ((I) Phase II).